Momentum-resolved dielectric response of free-standing mono-, bi-and tri- layer black phosphorus

Étienne Gaufrès, Frédéric Fossard, Vincent Gosselin, Lorenzo Sponza, François Ducastelle, Zhenglu Li, Steven G Louie, Richard Martel, Michel Côté, Annick Loiseau

Momentum-resolved dielectric response of free-standing mono-, bi- and tri-layer black phosphorus

Etienne Gaufrès[1,5]*, Frédéric Fossard[1], Vincent Gosselin[2], Lorenzo Sponza[1], François Ducastelle[1], Zhenglu Li[3,6], Steven G. Louie[3,6], Richard Martel[4], Michel Côté[2], and Annick Loiseau*[1]

[1] Laboratoire d'Etude des Microstructures, ONERA-CNRS, UMR104, Université Paris-Saclay, BP 72, 92322 Châtillon Cedex, France

[2] Département de physique, Université de Montréal, Montréal QC H3C 3J7, Canada

[3] Department of Physics, University of California at Berkeley, Berkeley, California 94720, USA

[4] Département de chimie, Université de Montréal, Montréal QC H3C 3J7, Canada

[5] Institut d'Optique & CNRS, LP2N UMR 5298, F-33400 Talence, France

[6] Materials Sciences Division, Lawrence Berkeley National Laboratory, Berkeley, California 94720, USA

*Correspondence to: annick.loiseau@onera.fr and etienne.gaufres@u-bordeaux.fr

Abstract

Black phosphorus (BP), a 2D semiconducting material of interest in electronics and photonics, exhibits physical properties characterized by strong anisotropy and band gap energy that scales with reducing layer number. However, the investigation of its intrinsic properties is challenging because thin layer BP are photo oxidized in ambient conditions and the energy of their electronic states shift in different dielectric environment. We prepared free-standing samples of few layer BP in glovebox conditions and probed the dielectric response in vacuum using Scanning Transmission Electron Microscopy and Electron Energy Loss Spectroscopy (STEM-EELS). Thresholds of the excitation energy are measured at 1.9 eV, 1.4 eV and 1.1 eV for the mono- bi- and tri-layer BP,

respectively and these values are used to estimate the corresponding optical band gaps. A comparison of our results with electronic structure calculations indicates that the variation of the quasi-particle gap is larger than that of the exciton binding energy. The dispersion of the plasmons *versus* momentum for 1-3 layer BP and bulk BP highlights a deviation from parabolic to linear dispersion and strong anisotropic fingerprints.

Introduction

Black phosphorus (BP) stands out from other 2D materials in the photonic and optoelectronic fields due to the high carrier mobility, about few thousands of $cm^2\ V^{-1}\ s^{-1}$ for holes, and a band gap that depends on layer thickness.[1-5] Composed of tetravalent phosphorus atoms in a quasi sp^3 hybridization, the puckered and lamellar structure of BP enables mechanical exfoliation of few layers BP, giving a modulation of the optical band gap from ~0.35 eV in the bulk BP to roughly 2 eV for the monolayer. [2,6,7] Additionally, the band gap remains direct for any layer number.[3,7,8] This unusual behavior in the panorama of 2D semiconductors is of high interest in various fields of photonics, such as light harvesting, climate monitoring (0.5 eV), telecommunication wavelengths (0.8 eV), and silicon photonics (1.1 eV).[9] Confinement effects in semiconducting nanomaterials induce, however, a significant renormalization of energy terms, which reshapes the dielectric response across the whole spectrum (0-30 eV) where interband transitions and plasmon resonances are found. In the case of ultrathin layers, the non-locality of the dielectric function can further tune the optical properties of nanomaterials and exacerbates material's sensitivity to environmental effects and dielectric surroundings.[10,11] Such effects are dominant for example in carbon nanotubes (1D) and exfoliated transition metal dichalcogenides (TMDC) (2D). [12-16] For few layers BP, it is therefore expected that both quantum confinement and interface effects influence the

optical response.[17,18] Hence, mapping the intrinsic dielectric response of ultrathin BP layers in reference conditions will provide the foundation for a key dataset of the optical response of BP and help predicting band gap energy with layer number in a complex dielectric environment, such as in BP-based Van der Waals (VdW) heterostructures.

Here, we measure the Energy Electron Loss Spectra (EELS) in the 1 - 30 eV range of mono-, bi-, tri-layer and bulk BP suspended in vacuum in a High-Resolution Transmission Electron Microscope (HRTEM) operated at 80 and 40 kV. A significant shift of the band gap threshold of freestanding samples is obtained compared to the reported values in other dielectric environments, such as SiO_2 and hexagonal boron nitride (h-BN). Using *ab-initio* Bethe-Salpeter simulations coupled to a variational model, we ascribe this shift to a strong layer dependent modulation of both the exciton binding energy, E_b, and the bandgap energy with the dielectric environment. For the BP monolayer, the amplitude of the modulation reaches up to 0.6 eV when the average environmental dielectric function varies from 1 to 40. Furthermore, the EELS responses of the surface and volume plasmons for 1-3 layers and bulk BP as a function of momentum show strong anisotropic confinement effects in the armchair and zigzag directions and specific fingerprints that are consistent with our *ab initio* results.

Experiments.

The dielectric response of few layers BP is probed using EELS signals acquired with a transmission electron microscope (Zeiss Libra 200 MC) equipped with an electrostatic CEOS monochromator, an in-column filter and a Gatan ultrascan 1000 CCD camera. The microscope operates at 40 or 80 kV to avoid knock-on damage and exhibits an energy resolution of 100 meV. To avoid layer degradation, black phosphorus samples are exfoliated in a glovebox with oxygen and moisture levels below 1 ppm using a PDMS stamp.[6] The thin

layers are then transferred from the stamp to an holey carbon TEM grid using direct contact (Supporting Information). The TEM grid is placed on the sample holder inside the glovebox and then transferred into the microscope under an inert atmosphere. The layer number is estimated using HRTEM phase contrast images and High Annular Angle Dark Field (TEM-HAADF) Z-contrast images following a procedure described in our previous work (Supporting Information).[6] During analysis, the flake is oriented to obtain the main crystallographic directions armchair [002] and zigzag [200] in the diffraction pattern ([010] zone axis) (Fig. 1a and 1c). In this configuration, an area of about 100 nm in diameter, free of eventual impurity and at a minimum distance of 30 nm from another flake or thickness change, is selected to perform the EELS experiments. (see supporting information, Figure S0)

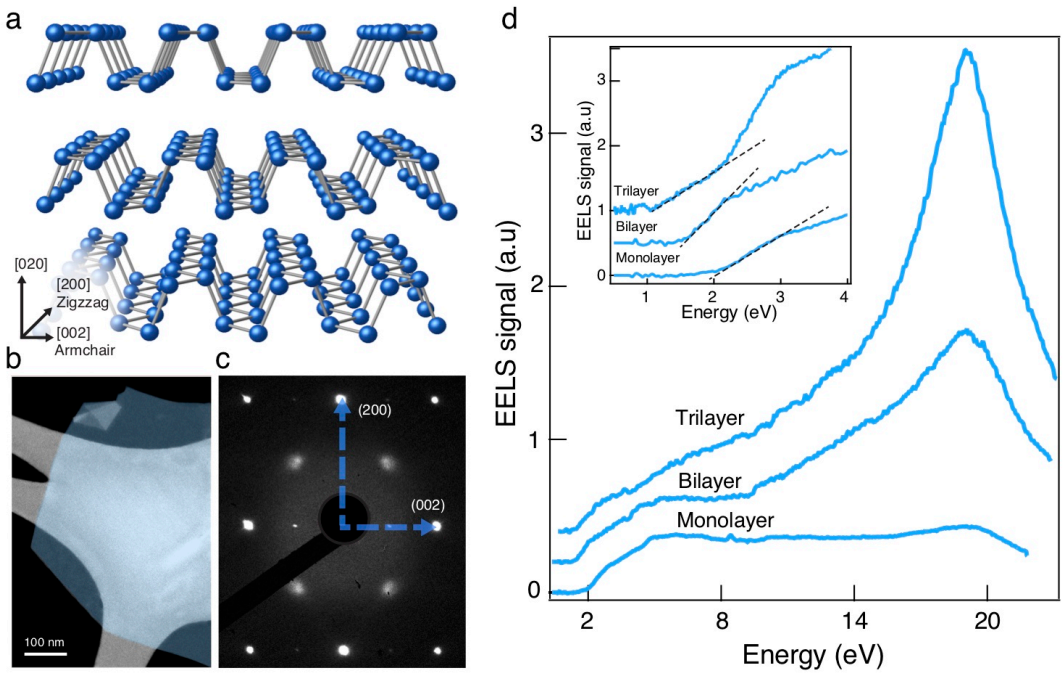

Figure 1. Crystallographic structure and EELS response of exfoliated BP suspended in vacuum**. (**a) Schematic description of the BP atomic structure and its crystallographic axis. (b) HAADF contrast image recorded at 80 kV of a bilayer BP exfoliated on a TEM grid. The layer is colored in blue for clarity. (c) Assignation of the armchair and zigzag orientations [002] and [200], respectively in the diffraction pattern recorded from an exfoliated few-layers BP. (d) Electron Energy Loss Spectroscopy (EELS) spectra at 80 kV in the range (1-23 eV) of

the mono- bi- tri-layers BP. Inset: High-resolution Valence-EELS (1-5 eV) spectra displaying thresholds at 1.9 eV, 1.4 eV, 1.1 eV for the mono-, bi-, tri-layer BP, respectively.

We first studied the impact of 2D quantum confinement on the valence band edge excitations of ultrathin BP layers suspended in vacuum. For that purpose, we selected freestanding layers displaying HAADF contrasts consistent of exfoliated BP samples having 1, 2 and 3 layers; as an example, the bilayer is illustrated in Fig. 1b. Note that measurements have been repeated on other samples with the same results (Figs. S1 to S9, Supporting Information). The EELS spectra in the range between 0 eV and 4 eV of the corresponding layers (inset of Fig 1d) are used to evaluate excitation threshold energies of 1.9±0.1 eV, 1.4±0.1 eV and 1.1±0.1 eV for 1, 2 and 3 layer BP, respectively using the tangential method, which is a standard analysis method applied to semiconductors.[19-25] As shown in the Supporting Information, this empirical method leads to reproductible values of the threshold (see in particular Figure S6). A comparison of these values with optical band gap energies, E_x, of few layers BP reported in the literature (Table S1, Supporting Information) indicates a slightly blue-shifted resonance of about 0.25 eV on average (Table S3, Supporting Information). At first sight, this discrepancy can be ascribed to the fundamental difference between EELS and optical spectroscopies. As further detailed in the Supplementary Information, we show, however, that the difference between band gap energy values obtained with EELS and optical absorption is negligible (within 0.1 eV at most) in the case of BP and that the blue shift measured here is mainly due to a difference in environmental screening. In short, the experimental optical absorption and EELS loss function are indeed intrinsically different, the former being proportional to $\mathrm{Im}[\varepsilon(\omega)]$ and the latter to $-\mathrm{Im}[1/\varepsilon(\omega)]$, but the magnitude of this difference depends on the strength of the excitonic effects: When the excitonic peak is strong and far from the continuum of interband transitions, such as in h-BN, the threshold of the two spectra may differ substantially. However, Kramers-Kronig relations imply similar structures between

EELS and absorption spectra when exitonic effects are weak. For BP layers, we evaluated this difference using values obtained by EELS as a reference input for calculations. To do so, we compared simulated spectra of $Im[\varepsilon(\omega)]$ and $-Im[1/\varepsilon(\omega)]$ in the mono-, bi-, and tri-layers BP by solving the Bethe-Salpeter equation (BSE) while quasiparticle effects have been included by shifting the Kohn-Sham empty states by an amount which ensures that the experimental thresholds match those extracted from the simulated loss function using the same tangential method. All parameters of the calculations can be found in the Supporting Information. As an example, this analysis carried out on the monolayer is shown in the inset of Fig. 2a, where blue arrows indicate the quasiparticle gap (E_g = 2.46 eV), and the optical gap derived from absorption spectra (peak of $Im[\varepsilon(\omega)]$). Note that the electronic band gap value obtained for the monolayer in vacuum is in very good agreement with the value recently predicted by Franck *et al.* by using many-body quantum Monte Carlo calculations.[26] In all three cases, the corresponding optical gap extracted from the loss function is less than 0.1 eV higher than the EELS threshold, which is within the experimental error bar. Therefore, we conclude that the measured EELS threshold values are representative of the optical gap energies of the freestanding BP layers considered here.

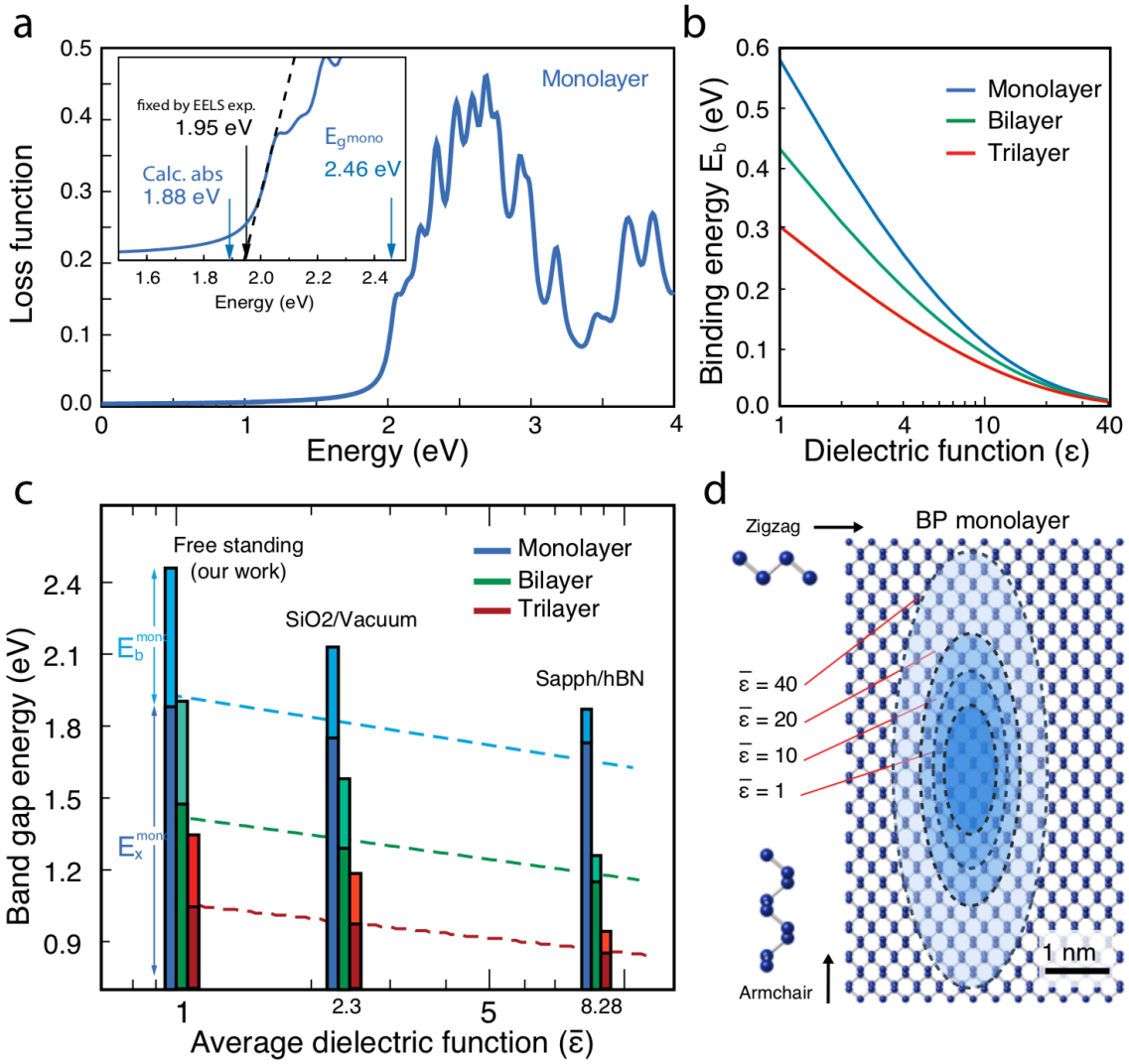

Figure 2. Dielectric screening effects on band gap and excitons binding energy in few layers BP. (a) BSE loss function of the monolayer. Inset: close up on the spectral onset. Arrows mark the energy gaps obtained by the same extrapolation method employed using the experimental EELS results (black arrow) and the calculated absorption peak (blue arrows). **(**b) Exciton binding energies as a function of the average environmental dielectric function $\bar{\varepsilon}$. (c) Optical gaps Ex (dark segments) and exciton binding energies Eb (light segments) in different dielectric environments. The optical gaps are experimental data coming from literature (see Table S3) and from this work. The dashed lines are linear interpolations of the experimental data to guide the eyes. (d) Representation of the simulated excitonic radii for the monolayer in the armchair and zigzag directions for different dielectric environments.

Ruling out the mismatch between EELS and optical absorption measurements and assuming that the dielectric screening of the surrounding can significantly impact the electronic band

gap and the binding energy, E_b, of the excitons, it appears that the 0.25eV blue shift of the threshold energies is due to the different dielectric environments between our freestanding samples and other samples in the literature, which are all supported on a substrate.. To test this hypothesis, we developed a variational model based on a generalization of the approach introduced by Prada *et al.*[27] that describes the excitons in a planar geometry. In our model, the system is composed of a thin slab of BP sandwiched between two semi-infinite dielectrics ε_1 and ε_2 , which contribute to the screening through an average dielectric function $\bar{\varepsilon}$ (see Supporting Information). We first computed $E_b(\bar{\varepsilon})$ and the calculations indicate a strong dependency of E_b on $\bar{\varepsilon}$ with a maximum amplitude variation of about 0.6 eV and 0.3 eV on the range $1<\bar{\varepsilon}<40$ for the mono-layer and tri-layer BP, respectively (Fig. 2b). Hence, the thinner the BP film, the stronger is the effect of screening by the environment on the optical properties. Furthermore, the impact of quantum confinement with reducing layer number on the excitonic properties vanishes when the dielectric environment provides strong screening. Consistently, the in-plane excitonic radii, a_x and a_y extracted from the model, increase for increasing $\bar{\varepsilon}$ due to reduced electron-hole attraction and their values are significantly different owing to the anisotropy of the system (Fig. 2d). These radii quantify the extension of the electron-hole pair in the two orthogonal directions and highlight the strong anisotropy of BP where the exciton is elongated along the armchair direction. In the model, this anisotropy is taken into account by the effective mass of the electron-hole pair μ_{eh}, which is larger for the zigzag direction (x) than for the armchair direction (y). Note also that the model predicts an anisotropy factor $\lambda=a_y/a_x$ almost constant in all environments for the three systems (around 2.5 in the monolayer and the bilayer, around 2.3 in the trilayer).

As shown in Fig. 2c and based on our experimental dataset and the optical gap values, $E_x(\bar{\varepsilon})$, found in the literature[7,28] (see also Table S3), a simulated abacus can be drawn to provide an

estimate of the quasiparticle gap ($E_g=E_x+E_b$) expressed as the sum of the optical gap (E_x) and the corresponding exciton energy (E_b) for various effective dielectric constants simulating various experimental conditions. This abacus enables to rationalize the already diverse experimental data published on few layers BP and show the strong impact of the surroundings on the optoelectronic properties of thin layers BP, which is relevant in the context of BP passivation or after integration in heterostructures.[29]

A usual assumption in the context of nano-objects is that the environmental dielectric screening significantly shifts the binding energy of the exciton and renormalizes the fundamental gap, and that these changes of opposite sign compensate almost exactly, resulting in a weak dependence of E_x on the (environmental) screening. This hypothesis has been put forward in theoretical works on carbon and h-BN nanotubes[30] and recently reaffirmed by Qiu *et al.* on free-standing and supported few-layer BP[18]. What emerges from our study, is that E_x decreases nevertheless with larger screening. Giving that dielectric effects in exfoliated BP drive changes of E_b and E_g, the reduction of E_g appears sizably larger than the reduction of E_b.

Dispersions of plasmons

In another set of experiments, we probed the dielectric response of ultrathin BP samples in the range 10-40 eV and its dispersion as a function of the momentum q. The details of our TEM apparatus for dispersive EELS recording can be found in Supporting Information and in the work by Fossard *et al.*[31] In Fig. 3a, we compared the dispersion of the dielectric response in the bilayer BP for two values of momentum close to 0, i.e. q = 0 Å^{-1} and q = 0.2 Å^{-1}. It appears clearly that the near band edge part of the dielectric response rapidly vanishes and

cannot be resolved with our setup. This is consistent with the selection rules related to optical processes for non-zero values of the momentum and with the exciton dispersion predicted for BP and other 2D materials.[32,33]

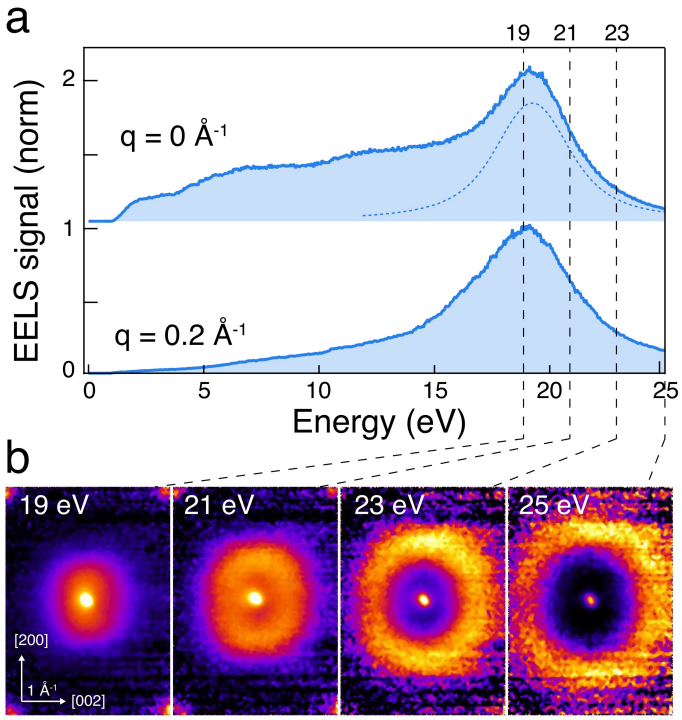

Figure 3. Energy Filtered TEM-EELS**.** (a) Momentum resolved EELS spectra at q = 0 Å^{-1} and q = 0.2 Å^{-1} from a bi-layer BP. (b) Energy-filtered scattering patterns (EFSP) measured at different energies in the plasmon dispersion range. Experiments done with an accelerating voltage of 80 kV.

Now, we focus on the dispersion of the plasmonic contributions, which is characterized by a maximum intensity at 19.3 eV (for q = 0 Å^{-1}), using the TEM in-column energy filter to record the scattering pattern at fixed energies (EFSP). Figure 3b shows the intensity repartition of the dielectric function as a function of momentum and direction for fixed values of energy. At 19 eV, the intensity maximum of the plasmon is consistently concentrated on values of q close to 0 Å^{-1}.[34,35] The extraction of the scattering pattern performed at higher energies, i.e. E = 21, 23 and 25 eV, reveals a significant dispersion of the maximum intensity

with an elongated donut shape in the zigzag direction (i.e. [200]). This feature highlights the impact of the structural anisotropy of BP on the plasmon dispersion.

To better scrutinize this anisotropic fingerprint in the plasmonic dispersion, we performed ω-q map according to a TEM configuration reported in reference[31] with an energy and momentum resolution of 0.1 eV and 0.1 $Å^{-1}$, respectively. As an example, the ω-q map of bulk BP losses along the armchair direction is plotted in Fig. 4a. The intensity of the raw EELS signal is corrected by a q^2 factor, which comes from the nature of the recorded signal $S(q) = -(1/q^2)$ $Im(1/\varepsilon)$. For clarity, an offset is also applied so that the figure doesn't display a black line at $q = 0$. The two branches of the plasmon dispersion are clearly identified, even beyond the Brillouin zone limit, and characterized by an amplitude shift of more than 5 eV. Thanks to the in-plane rotation of the specimen holder, we repeated the experiment after rotating the same flake in the TEM chamber by an in-plane angle of 90° to record the contributions in the zigzag direction. From the EFSP or ω-q experiments, the plasmon spectra were extracted from the datacube, as demonstrated in Fig. 4b, for a tri-layer BP.

In Fig. 4c, the plasmon dispersion for the mono-, bi-, tri-layer and bulk are compared together. Each dotted point corresponds to the position of the plasmon energies along the armchair and zigzag directions. In a complementary way, we also calculated the EELS response of bulk and monolayer BP by directly computing the dielectric function using a first-principles approach in the following way. First, the ground state electronic structure is obtained with the ABINIT code[36] and then the electronic states are processed by the GW Berkeley code[37] in order to compute the dielectric response of the system within the random phase approximation. We then extract the momentum and frequency dependence of the dielectric function. The red crosses correspond to the plasmon energies calculated in the bulk

and show good agreement with experimental data. The features of the plasmon dispersions presented in Figure 4c are therefore identified as being intrinsic of bulk BP material.

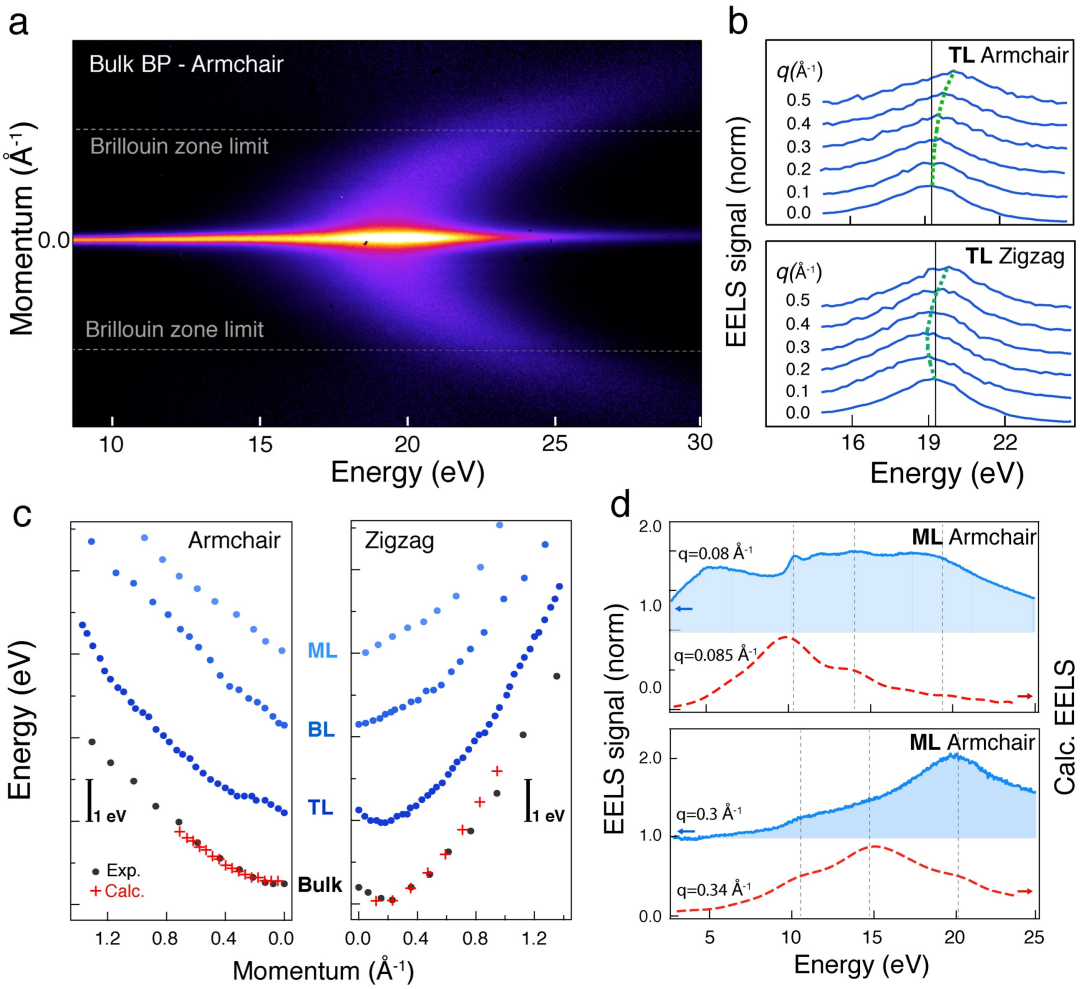

Figure 4. Plasmon dispersion in the armchair and zigzag directions in few-layers BP. (a) *ω-q* map of the plasmon losses centered at 19.3 eV along the armchair direction. (b) Momentum resolved plasmon losses extracted from *w-q* experiments of a tri-layers BP along the armchair (top) and zigzag (bottom) directions. (c) Maximum volume plasmon peak energy as function of momentum and crystallographic orientations (armchair and zigzag). The data are extracted

from the *w*-*q* maps recorded from exfoliated mono- bi- tri-layers BP (ML, BL, TL) and bulk BP. The simulated data for the bulk are indicated by red crosses. The ML, BL, TL and bulk dispersions are up-shifted for clarity. (d) Measured (continuous blue) and calculated (dashed red) EELS signals of mono-layer BP for q ~ 0 $Å^{-1}$ and q ~ 0.3 $Å^{-1}$.

These results of the dispersion present clear deviations from the well-known parabolic $\sqrt{q}$ dependency of a plasmon dispersion in 2D systems, with specific fingerprints compared to bulk for the armchair and zigzag directions for monolayer and bilayer BP. First, the dispersion amplitude is asymmetrically higher for the zigzag direction than for the armchair direction. As already put forward for accounting for the anisotropic extension of excitons in Fig.2c, this anisotropy of the EELS response corroborates the theoretical prediction by Gosh *et al*. obtained using the TDDFT framework[38] that it is most likely linked to the difference of effective mass between the main orthogonal directions.[39] Second, another non-parabolic behavior and asymmetric inversion centers of the dispersion in the range of 0 $Å^{-1}$ – 0.3 $Å^{-1}$ are identified for the zigzag direction, as highlighted in Figure 4b. Still present for tri-layer BP, the origin of this unexpected deviation is unclear but could be induced by an effective inter-band coupling promoted because of the small values of the bulk-like band gap energies.[39] This hypothesis is supported by the fact that this deviation, is quite attenuated in the bilayer and monolayer for which the bandgap energies (1.45 eV and 1.9 eV respectively) are much larger compared to bulk BP (0.35 eV) and even so for the trilayer (1.1 eV). Therefore, the attenuation of the non-parabolic behavior in mono and bilayer samples appears to be a fingerprint of the important change in band gap. It also means that plasmonic properties of BP films behave as bulk above 3 layers.

The electronic dispersion of the bilayer also stands out from that of the trilayer and bulk by the apparent loss of the parabolic dispersion towards a linearization of the plasmon dispersion. This quantum confinement effect was already observed in low-dimensional materials such as

carbon nanotubes and graphene by Kramberger *et al*.[40] For high momentum values, i.e. interaction distances of few Angstroms representing small fractions of the film thickness, the suppression of the neighboring effect in bilayer and monolayer may induce this linearization of the dispersion of plasmons.

Last, the plasmon response of a monolayer BP suspended in a vacuum shown in Fig. 4d is now discussed in more detail using support from calculated spectra. The EELS spectra for near-zero values of momentum in the armchair direction shows a strong decrease of the contribution from the volume plasmon at 19.3 eV compared to the near-band-edge contribution (1-5 eV). This is consistent with a volume plasmon vanishing when the thickness approaches zero values. Another feature in Fig. 4d is the very broad heterogeneous signal starting from 10 eV to 20 eV with structuration at 10 eV and 14 eV. This signal is also noticeable, although weaker, in the bilayer EELS spectra presented in Fig. 3a. The contribution at 10 eV has been observed in thin BP layers by Wu et al. and ascribed to high energy surface plasmons.[34] In comparison, the calculated EELS spectrum shows clear plasmonic contributions at 10 eV and 13.5 eV, which are coupled to a weak and broad contribution at around 20 eV. Besides the relative intensity, the positions of these features are in agreement with our experimental data. When comparing the experimental and simulated EELS responses of the monolayer for a momentum value of 0.3 $Å^{-1}$ (Fig. 4d bottom), it appears that the relative intensities of the contributions are modulated and that the decrease of the near-band-edge signal is effective with the main contribution at 20 eV and two minor contributions at 11 eV and 15 eV, shifted by about 1 eV compared to the spectra at $q \sim 0$ $Å^{-1}$. This shift is similar to those observed for the mono-, bi-, tri-layer and bulk BP dispersions with an average dispersion rate of 4 eV per $Å^{-1}$ with also a clear linearization effect between 0 and 1 $Å^{-1}$, comparable to what already noticed for the bilayer. (Fig. 4c) The simulation also

shows a similar shift of the surface and volume plasmon contributions in the EELS spectra calculated at 0.34 $Å^{-1}$, but with a less intense modulation of the relative intensity between surface *versus* volume contributions.

In conclusion we have measured the dielectric response of free standing BP layers using EELS spectroscopy in the range 1 - 40 eV. We found optical band gap thresholds of 1.9 eV, 1.4 eV and 1.1 eV for the mono- bi- and trilayer BP, respectively. The experimental data are simulated to determine the quasiparticle gap (E_g), the optical gap (E_x) and the corresponding exciton binding energy (E_b) for various effective dielectric constants, which provide an abacus of the optical response of BP as a function of dielectric environment. The variation of the electronic gap in few layer BP is found to be sizably larger than the variation of the binding energy. In bulk BP, experimental and calculated plasmon dispersions along the two orthogonal directions display a significant anisotropy both in amplitude and shape. A progressive linearization of the dispersion of the volume and surface plasmons is observed in both experimental and theoretical data of monolayer and bilayer BP. These results highlight the importance of strong quantum confinement effects in the optical properties of thin layer BP and pave the way for tuning them by tailoring the dielectric environment.

Methods

The black phosphorus crystal used in this work were purchased to HQ Graphene. BP was stored and exfoliated in a glovebox with regenerated Ar system to maintain the oxygen and moisture concentrations below 1ppm. Exfoliation of BP and the transfer of the flake on a TEM grid were performed using PDMS stamps (Syglard 184) cured at 70°C during 25 mins. (details in the supplementary) We used 300 mesh Holey carbon on a copper grid with mark to localize the flakes. The TEM grid is then placed on a tilt-rotation sample holder inside the

glovebox. The sample holder is finally sealed in a custom transfer plastic bag with a 40 mbar pressure of Ar and transferred to the TEM chamber for experiments.

Acknowledgments

This work received funding from the European Union's Horizon 2020 research and innovation program under grant agreements No. 696656 (Graphene Core 1) and No 785219 (Graphene Core 2) and from the ANR french program under the grant agreement N° ANR-17-CE24-0023-01 (EPOS-BP). E.G. acknowledges funding from the Marie-Skłodowska-Curie-IF 706476-BrightPhoton, the GDR-I Graphene and Co and the GDR-I multifunctional nanomaterials for travel support. V.G. and M.C. would like to acknowledge the support the Fonds de Recherche du Québec - Nature et Technologie (FRQNT), the Natural Sciences and Engineering Research Council of Canada (NSERC) under grants RGPIN-2016-06666. R. M. acknowledge support from Canada Research Chair and NSERC Discovery Programs. Part of the simulations were performed on computers provided by the Canadian Foundation for Innovation, the Ministère de l'Éducation des Loisirs et du Sport (Québec), Calcul Québec, and Compute Canada. Z.L. and S.G.L. acknowledge support from the Van der Waals Heterostructures program (KCWF16) at the Lawrence Berkeley National Lab through the Office of Science, Office of Basic Energy Sciences, Materials Sciences and Engineering Division, the U.S. Department of Energy under Contract No. DE-AC02-05CH11231, which provided for the calculations of dielectric responses using the BerkeleyGW package. The advanced computational methods and codes were provided by the Center for Computational Study of Excited-State Phenomena in Energy Materials (C2SEPEM) funded by the U.S. Department of Energy, Office of Basic Energy Sciences, Materials Sciences and Engineering Division, under Contract No. DE-AC02-05CH11231 at

the Lawrence Berkeley National Laboratory, as part of the Computational Materials Sciences Program.

Authors Contributions

E.G., F.F. performed the experiments, E.G., F.F., A.L., R.M. designed the experiments and analysed the results, E.G. prepared the samples, V.G., L.S., F.D., M.C., Z.L., S.G.L. performed the simulations, E.G and A.L. supervised the work. All authors contributed to the scientific discussions, manuscript preparation and final version.

References

(1) Li, L.; Yu, Y.; Ye, G. J.; Ge, Q.; Ou, X.; Wu, H.; Feng, D.; Chen X. H.; Zhang, Y. Black phosphorus field effect transistors. *Nat. Nanotech*. **2014**, 9, 372-377

(2) Qiao, J.; Kong, X.; Hu, Z.-X.; Yang, F.; Ji, W. High-mobility transport anisotropy and linear dichroism in few layer black phosphorus. *Nat. Comm*. **2014**, 5, 4475

(3) Liu, H.; Neal, A. T.; Zhu, Z.; Luo, Z.; Xu, X.; Tomanek, D.; Ye, P. D. Phosphorene, An unexpected 2D semiconductor with a high hole Mobility. *ACS Nano* **2014,** 8, 4, 4033-4041

(4) Tayari, V.; Hemsworth, N.; Kakih, I.; Favron, A.; Gaufrès, E.; Gervais, G.; Martel, R.; Szkopek, T. Two-dimensional magnetotransport in a black phosphorus naked quantum well. *Nat. Comm*. **2015**, 6, 7702

(5) Long, G.; Maryenko, D.; Shen, J.; Xu, S.; Hou, J.; Wu, Z.; Wong, W. K.; Han, T.; Lin, J.; Cai, Y.; Lortz R.; Wang, N. Achieving ultrahigh carrier mobility in two-dimensional hole gas of black phosphorus. *Nano Lett.* **2016**, 16, (12), 7768-7773

(6) Favron, A.; Gaufrès, E.;, Fossard, F.; Phaneuf-L'Heureux, A.-L.; Tang, Y-W.; Levesque, P.; Loiseau, A.; Leonelli, R.; Francoeur, S.; Martel, R. Photo-oxidation and quantum confinement effects in exfoliated black phosphorus. *Nat. Mater*. **2015,** 14, 826–832

(7) Li, L.; Kim, J.; Jin, C.; Ye, G. J.; Qiu, D. Y.; da Jornada, F. H.; Shi, Z.; L. Chen, L.; Zhang, Z.; Yang, F.; Watanabe, K.; Taniguchi, T.; Ren, W.; Louie, S. G.; Chen, X. H.; Zhang, Y.; Wang, F. Direct observation of the layer-dependent electronic structure in phosphorene. *Nat. Nanotech*. **2017**, 12, 21-25

(8) Wang, X.; Jones, A. M.; Seyler, K. L.; Tran, V.; Jia, Y.; Zhao, H.; Wang, H.; Yang, L.; Xia, F. Highly anisotropic and robust excitons in monolayer black phosphorus. *Nat. Nanotech*. **2015**, 10, (6), 517-521

(9) Thomson, D.; Zilkie, A.; Bowers, J. E.; Komljenovic, T.; Reed, G. T.; Vivien L.; Marris-Morini, D.; Cassan, E.; Virot, L.; Fédéli, J.-M.; Hartmann, J.-M.; Schmid, J. H.; Xu, D.-X.; Boeuf, F.; O'Brien, P.; Mashanovich, G. Z.; Nedeljkovic, M. Roadmap on silicon photonics. *J. Opt*. **2016**, 18, 073003

(10) Raja, A.; Chaves, A.; Yu, J.; Arefe, G.; Hill, H.M.; Albert F. Rigosi, A.F.; Berkelbach, T.C.; Nagler, P.; Schüller, C.; Korn, T.;Nuckolls, C.; Hone, J.; Brus, L.E.; Heinz, T.F.; Reichman, D.R.; Chernikov, A. Coulomb engineering of the bandgap and excitons in two-dimensional materials. *Nat. Commun*. **2017**, 8, 15251

(11) Gerber, I.C.; Marie, X. Dependence of band structure and exciton properties of encapsulated WSe_2 monolayers on the hBN-layer thickness. *Phys. Rev. B*. **2018**, 98, 245126

(12) Walsh, A. G.; Vamivakas, A. N.; Yin, Y.; Cronin, S. B.; Ünlü, M. S.; Goldberg B. B.; Swan, A. Screening of excitons in single, suspended carbon nanotubes. *Nano Lett*. **2007**, 7 (6), 1485-1488

(13) Aspirate, L.; McCulley, D. R.; Bertoni, A.; Island, J. O.; Ostermann, M.; Rontani, M.; A. Steele, G.; Minot, E. D. Giant modulation of the electronic band gap of carbon nanotubes by dielectric screening. *Scientific Reports* **2017**, 7, 8828

(14) Scheuscher, N.; Ochedowski, O.; Kaulitz, A. –M.; Gillen, R.; Schleberger, M.; Maultzsch, J. Photoluminescence of freestanding single- and few-layer MoS_2. *Phys. Rev. B* **2014**, 89, 125406

(15) Lin, Y.; Ling, X.; Huang, S.; Hsu, A. L.; Lee, Y. –H.; Kong, J.; Dresselhaus, M. S.; Palacios, T. Dielectric screening of excitons and trions in single layer MoS_2. *Nano Lett.* **2014**, 14, (10), 5569-5576

(16) Stier, A. V.; Wilson, N. P.; Clark, G.; Xu, X.; Crooker, S. A. Probing the influence of dielectric environment on excitons in monolayer WSe_2: Insight from high magnetic fields. *Nano Lett.* **2016**, 16, (11), 7054-7060

(17) Deng, Y.; Luo, Z.; Conrad, N. J.; Lui, H.; Gong, Y.; Najmaei, S.; Ajayan, P. M.; Lou, J.; Xu, X.; Ye, P.D. Black phosphorus - monolayer MoS2 van der Waals Heterojunction p-n diode. *ACS Nano* **2014**, 8, (8) 8292-8299

(18) Qiu, D. Y.; da Jornada, F. H.; Louie, S.G. Environmental screening effect in 2D materials, Renormalization of the band gap, electronic structure and optical spectra of few layer black phosphorus. *Nano Lett.* **2017**, 17, (8) 4706-4712

(19) Brockt G.; Lakner, H. Nanoscale EELS analysis of dielectric function and bandgap properties in GaN and related materials. *Micron* **2000**, 31, 435-440

(20) Erni, R.; Browning, N. D. Quantification of the size-dependent energy gap of individual CdSe quantum dots by valence electron energy-loss spectroscopy. *Ultramicroscopy* **2007**, 107, 267-273

(21) Virdi, K. S.; Kauffmann, Y.; Ziegler, C.; Ganter, P.; Blaha, P.; Lotsch, B. V.; Kaplan W. D.; Scheu, C. Band gap extraction from individual two dimensional perovskite nanosheets using valence electron energy loss spectroscopy. *J. Phys. Chem. C* **2016**, 120, 11170-11179

(22) Park, J.; Heo, S.; Chung, J. –G.; Kim, H.; Lee, H.; Kim, K.; Park, G. –S. Bandgap measurement of thin dielectric films using monochromated STEM-EELS. *Ultramicroscopy* **2009**, 109, 9, 1183-1188

(23) Tizei, L. H. G.; Lin, Y. –C.; Mukai, M.; Sawada, H.; Lu, A. –Y.; Li, L. –J.; Kimono K.; Suenaga, K. Exciton mapping at subwavelength scales in two-dimensional materials. *Phys. Rev. Lett.* **2015**, 114, 107601

(24) Dileep, K.; Sahu, R.; Sarkar, S.; Peter S. C.; Dalta, R. Layer specific optical band gap measurement at nanoscale in MoS2 and ReS2 van der Waals compounds by high resolution electron energy loss spectroscopy. *J. Appl. Phys. Lett.* **2016**, 119, 114309

(25) Williams, D. B.; Carter, C. B. Transmission Electron Microscopy, a Textbook for Materials Science; **2009** Part 3: Imaging, Chapter 22; Springer Science + Business Media: New York, 379−388

(26) Frank, T.; Derian, R.; Tokár, K.; Mitas, L.; Fabian, J.; Štich, I. Many-body quantum Monte Carlo study of 2D materials: Cohesion and bandgap in single-layer phosphorene. *Phys. Rev.* X **2019**, 9, 011018

(27) Prada, E.; Alvarez, J. V.; Narasimha-Acharya, K. L.; Bailen, F. J.; Palacios, J. J.; Effective-mass theory for the anisotropic exciton in two-dimensional crystals: Application to phosphorene. *Phys. Rev. B* **2015**, 91, 245421

(28) Yang, J.; Xu, R.; Pei, J.; Myint, Y. W.; Wang, F.; Wang, Z.; Yu, Z.; Lu, Y.; Unambiguous identification of monolayer phosphorene by phase-shifting interferometry. *arXiv* **2014**, 1412:6701

(29) Kern, L.-M.; Galceran, R.; Zatko, V.; Galbiati, M.; Godel, F.; Perconte, D.; Bouamrane, F.; Gaufrès, E.; Loiseau. A.; Brus, P.; Bezencenet, O.; Martin, M.-B.; Servet, B.; Petroff, F.; Dlubak, B.; Seneor, P. Atomic layer deposition of a MgO barrier for passivated black phosphorus spintronics platform. *Appl. Phys. Lett*. **2019,** 114, 5, 053107

(30) Wirtz, L.; Marini, A.; Rubio, A. Excitons in boron nitride nanotubes: Dimensionality effects. *Phys. Rev. Lett*. **2006**, 96, 126104

(31) Fossard, F.; Sponza, L.; Schué, L.; Attaccalite, C.; Ducastelle, F.; Barjon, J.; Loiseau, A. Angle-resolved electron energy loss spectroscopy in hexagonal boron nitride. *Phys. Rev. B* **2017**, 96, 115304

(32) Hong, J.; Li, K.; Jin, C.; Zhang, X.; Zhang, Z.; Yuan, J. Layer-dependent anisotropic electronic structure of freestanding quasi-two-dimensional MoS_2. *Phys. Rev. B* **2016**, 93, 075440

(33) Wachsmuth, P.; Hambach, R.; Kinyanjui, M. K.; Guzzo, M.; Benner, G.; Kaiser, U. High-energy collective electronic excitations in free-standing single-layer graphene. *Phys. Rev. B* **2013**, 88, 075433

(34) Wu, R. J.; Topsakal, M.; Low, T.; Robbins, M. C.; Haratipour, N.; Jeong, J. S.; Wentzcovitch, R. M.; Koester, S. J.; Mkhoyan, K. A. Atomic and electronic structure of exfoliated black phosphorus. *J. Vac. Sci. Technol A* **2015**, 33, 060604

(35) Nicotra, G.; van Veen, E.; Deretzis, I.; Wang, L.; Hu, J.; Mao, Z.; Fabio, V.; Spinella, C.; Chiarello, G.; Rudenko, A.; Yuan, S.; Politano, A. Anisotropic ultraviolet-plasmon dispersion in black phosphorus. *Nanoscale* **2018**, 10, 21918-21927

(36) Gonze, X. et al. Recent Developments in the ABINIT Software Package. *Comput. Phys. Commun.* **2016**, 205, 106–310

(37) Deslippe, J.; Samsonidze, G.; Strubbe, D. A.; Jain, M.; Cohen, M. L.; Louie, S. G. BerkeleyGW: A Massively Parallel Computer Package for the Calculation of the Quasiparticle and Optical Properties of Materials and Nanostructures. *Comput. Phys. Commun*. **2012**, 183, 1269

(38) Gosh, B.; Kumar, P.; Thakur, A.; Chauhan, Y. S.; Bhowmick, S.; Agarwal, A. Anisotropic plasmons, excitons and electron energy loss spectroscopy of phosphorene. *Phys. Rev. B* **2017**, 96, 035422

(39) Low, T.; Roldàn R.; Wang, H.; Xia, F.; Avouris, P.; Moreno, L. M.; Guinea, F. Plasmons and screening in monolayer and multilayer black phosphorus. *Phys. Rev. Lett*. **2014**, 113, 106802

(40) Kramberger, C.; Hambach, R.; Giorgetti, C.; Rümmeli, M.H.; Knupfer, M.; Fink, J.; Bücher, B.; Reining, L.; Einarsson, E.; Maruyama, S.; Sottile, F.; Hannewald, K.; Olevano, V.; Marinopoulos, A.G.; Pichler, T. Linear plasmon dispersion in single wall carbon nanotubes and the collective excitation spectrum of graphene. *Phys. Rev. Lett*. **2008**, 100, 196803

Supporting information file for

Momentum-Resolved Dielectric Response of Free-Standing Mono-, Bi- and Tri- Layer Black Phosphorus

Etienne Gaufrès[1,5]*, Frédéric Fossard[1], Vincent Gosselin[2], Lorenzo Sponza[1], François Ducastelle[1], Zhenglu Li[3,6], Steven G. Louie[3,6], Richard Martel[4], Michel Côté[2], and Annick Loiseau*[1]

[1] Laboratoire d'Etude des Microstructures, ONERA-CNRS, UMR104, Université Paris-Saclay, BP 72, 92322 Châtillon Cedex, France

[2] Département de physique, Université de Montréal, Montréal QC H3C 3J7, Canada

[3] Department of Physics, University of California at Berkeley, Berkeley, California 94720, USA

[4] Département de chimie, Université de Montréal, Montréal QC H3C 3J7, Canada

[5] Institut d'Optique & CNRS, LP2N UMR 5298, F-33400 Talence, France

[6] Materials Sciences Division, Lawrence Berkeley National Laboratory, Berkeley, California 94720, USA

*Correspondence to: annick.loiseau@onera.fr and etienne.gaufres@u-bordeaux.fr

Summary

1- Exfoliation and TEM grid preparation.

The TEM grids with BP were prepared in a glovebox with O_2 and H_2O partial pressure kept below 1ppm, as follows. The BP crystal (HQ graphene) was exfoliated using two slabs of PDMS. Then a TEM grid (copper, Holley carbon 300 mesh) is softly sandwiched between the two PDMS stamp to transfer some BP flakes on the grid. Then the grid is placed on double tilt TEM sample holder, previously inserted in the glove box. To avoid contamination and photooxidation of the flakes during the transfer to the TEM, the sample holder is sealed inside the glovebox by using a thermo-plastic bag. This bag wall is safely maintained on the TEM chamber hole and opened just before inserting the TEM sample holder.

2- Layer number determination based on HAADF Z-contrast.

2.1 Determination of the region-of-interest on a BP flake for EELS experiments

The presence of another flake or a change in thickness close to the probed area can strongly affect the EELS results. The Figure S0 presents an experiment, in witch a periodic recording of the EELS spectra along a line scan is performed, starting from vacuum, out of the flake to few nm inside the flake (aloof experiment). The spot-size of the electron beam is roughly 1.5-2 nm. As a results we observed that the electron beam senses the flake in the low loss regime until a distance of 15-20 nm from the flake, due to the electric field induced by the electron beam. We also noticed that the plasmon resonances are only excited when the beam is focused on the flake. In consequence we took a special care in positioning the beam probe at a minimum distance of 30 nm of another object, to avoid an eventual contamination of the loss signal.

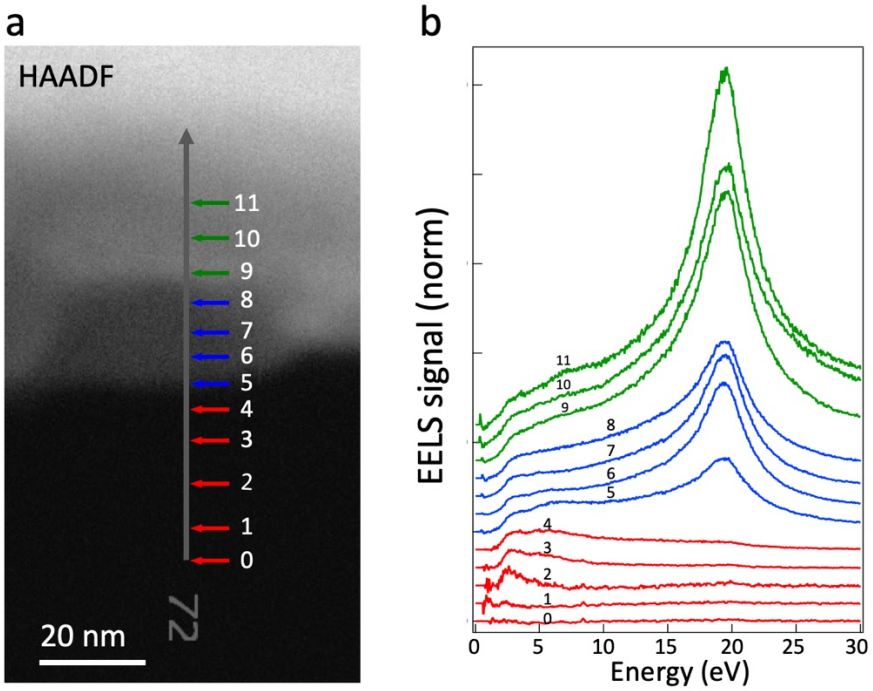

Figure S0: **a** HAADF image of a free-standing flake of BP exfoliated on TEM grid. The grey arrow indicates the line-scan direction. The coloured and numerated arrows point the positions of the beam positions for recording the EELS spectra displayed in panel (**b**). HAADF image and EELS spectra recorded at 80kV.

2.2 Analysis of the HAADF images for the layer number determination.

We have used the same calibration procedure that we used in the paper by Favron *et al* (Nature Materials (2015)). We have relied on the Z-contrast HAADF signal to measure the quantity of matter that interacts with the electron beam. Indeed, HAADF signals are directly related to the number of atoms and to the atomic number and the signal follows a power law, which makes it very sensitive to thickness. Further, the frequent observation of folded layers is very precious as it furnishes an internal calibration of the dependence of the HAADF intensity to the flake thickness. An example can be seen in Figure S1. A 3L part of the flake is folded (zone labelled 3L+3L) providing an internal thickness metrics.

In all cases, the zones selected for EELS measurements were at least over 100 nm in lateral size, so that they are solely illuminated by the electron beam both in EFTEM mode and in STEM mode for w-q mapping acquisition and that EELS signal is not polluted by proximity effect from the surrounding of the zone of interest.

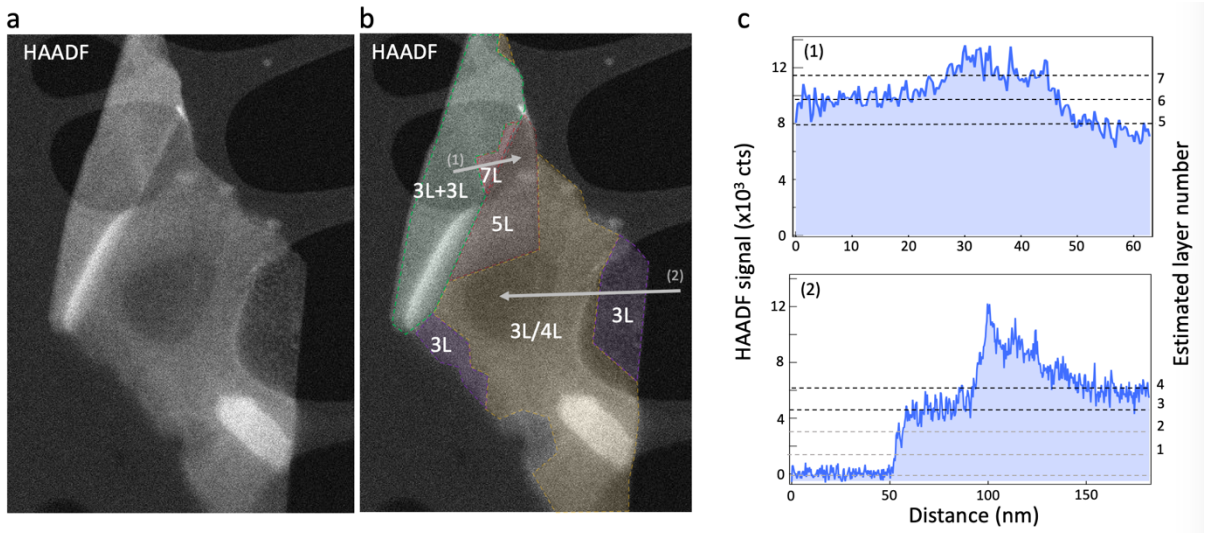

Figure S1. **a** HAADF image recorded at 80 kV of an exfoliated black phosphorus flake deposited on holey carbon TEM grids. b Same HAADF image as in **a** with a layer number indication using semi-transparent colour code based on the analysis of the HAADF profiles indicated by the numerated grey arrows and presented in panel **c**. The suspended trilayer was labelled trilayer 1 for the EELS experiment.

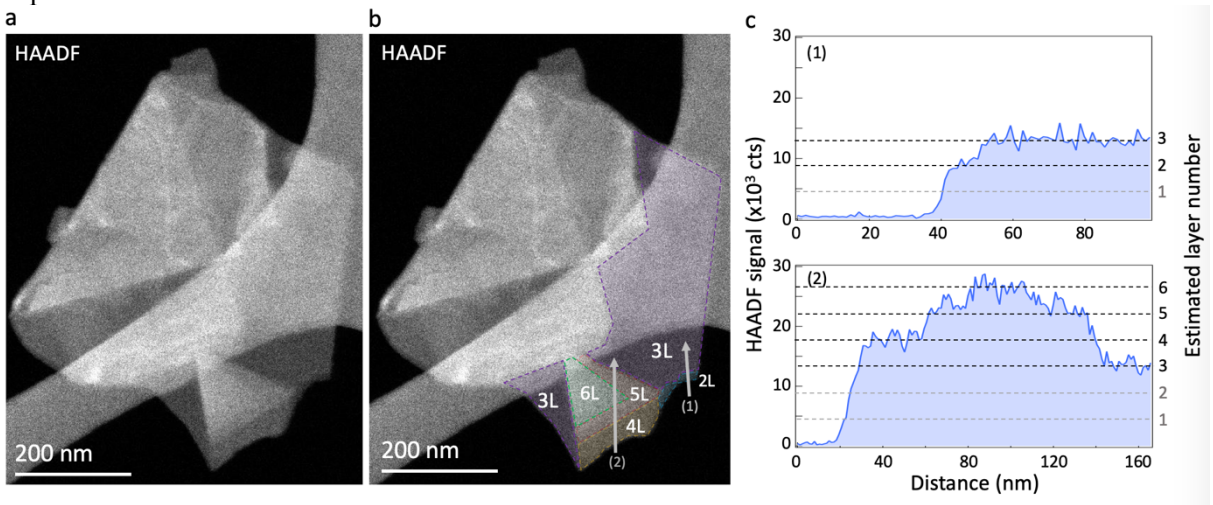

Figure S2. **a** HAADF image recorded at 80 kV of an exfoliated black phosphorus flake deposited on holey carbon TEM grids. b Same HAADF image as in **a** with a layer number indication using semi-transparent colour code based on the analysis of the HAADF profiles indicated by the numerated grey arrows and presented in panel **c**. The suspended trilayer was labelled trilayer 2 EELS experiment.

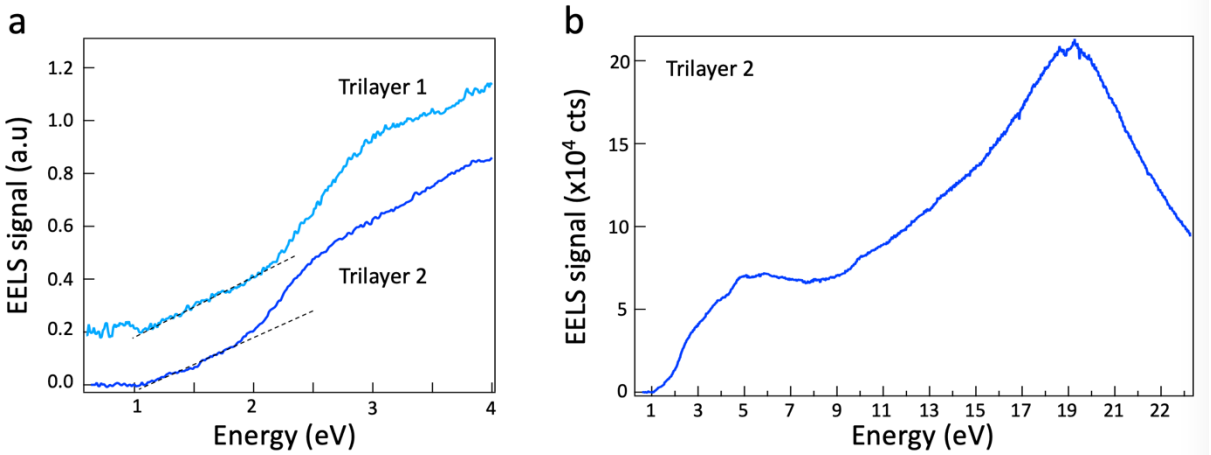

Figure S3. **a** EELS spectrum of trilayer 1 and trilayer 2 shown in Figures S1 and S2. from 0.6 eV to 4 eV. **b** EELS spectra of trilayer 2 recorded at 80kV from 0.6 eV to 22 eV. Spectra recorded at 80kV.

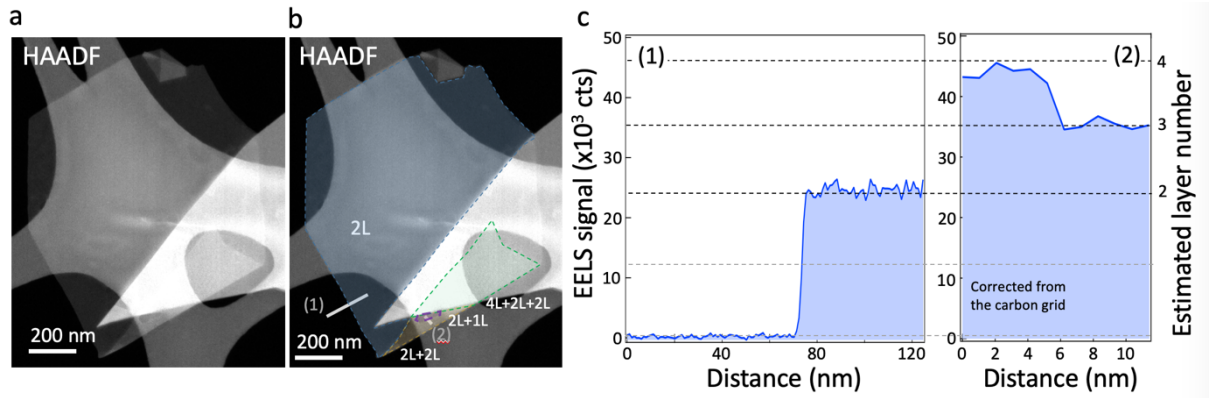

Figure S4. **a** HAADF image recorded at 80 kV of an exfoliated black phosphorus flake deposited on holey carbon TEM grids. b Same HAADF image as in **a** with a layer number indication using semi-transparent colour code based on the analysis of the HAADF profiles indicated by the numerated grey bars and presented in panel **c**. The suspended bilayer was labelled bilayer 1 for the EELS experiment.

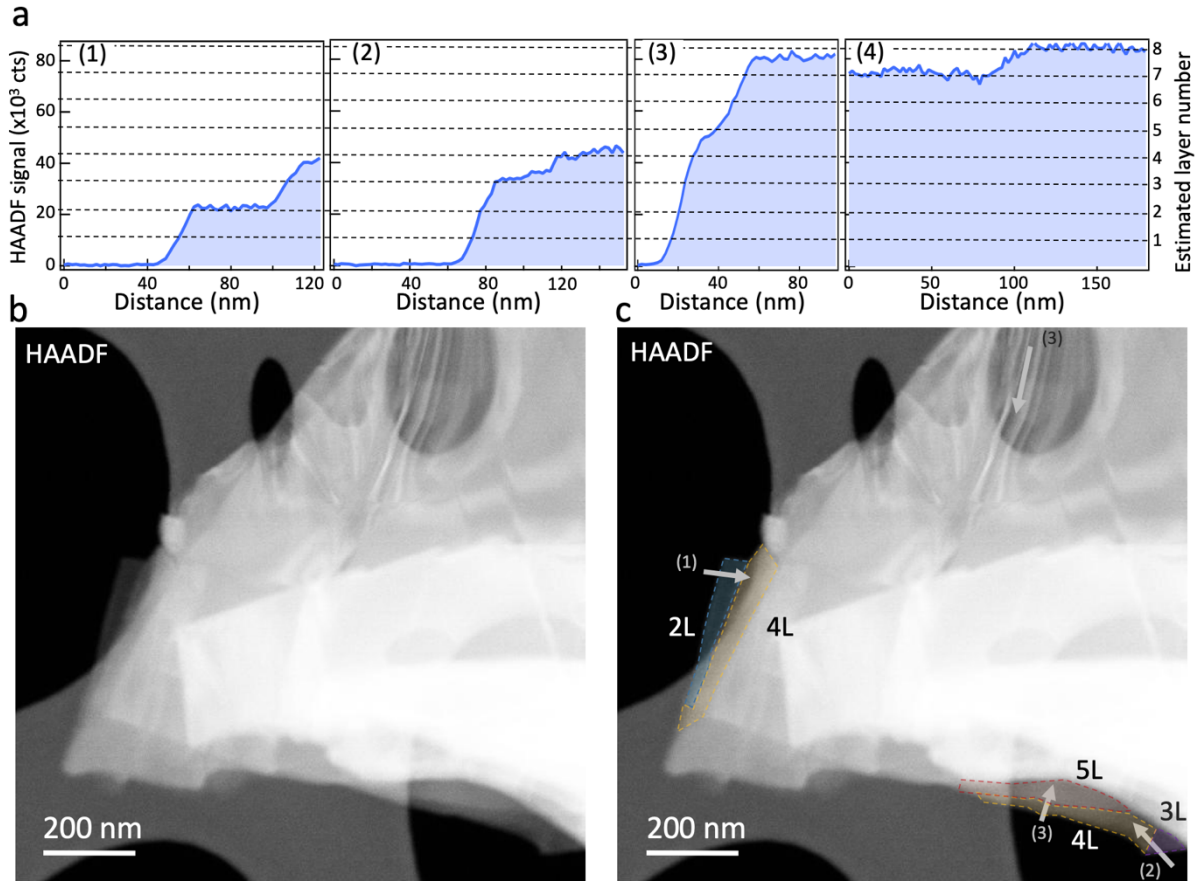

Figure S5. **a** HAADF image recorded at 80 kV of an exfoliated black phosphorus flake deposited on holey carbon TEM grids. b Same HAADF image as in **a** with a layer number indication using semi-transparent colour code based on the analysis of the HAADF profiles indicated by the numerated grey bars and presented in panel **c**. The suspended bilayer was labelled bilayer 2 for the EELS experiment.

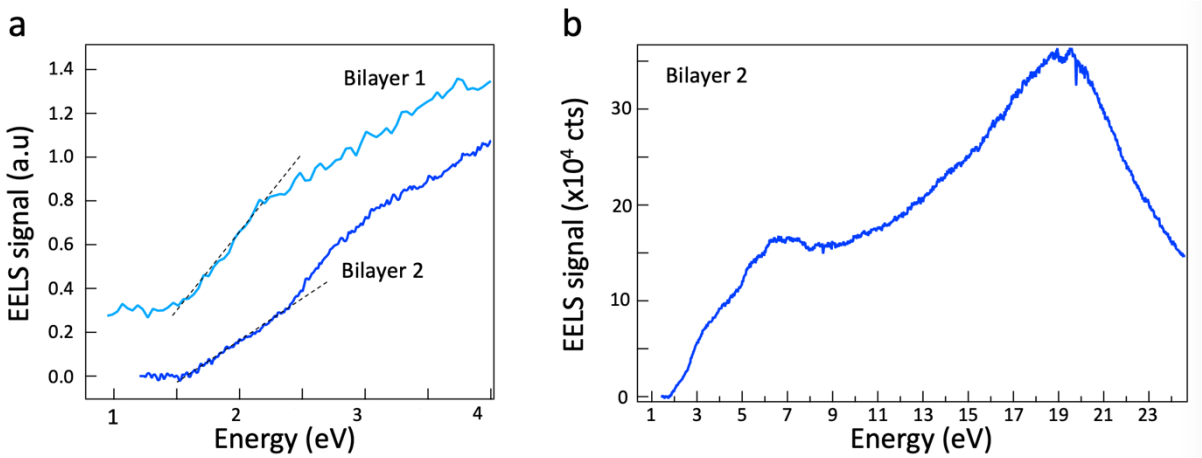

Figure S6. **a** EELS spectrum of bilayer 1 and bilayer 2 shown in Figures S1 and S2. from 0.6 eV to 4 eV. **b** EELS spectra of bilayer 2 recorded at 80kV from 1 eV to 24 eV. Spectra recorded at 80kV.

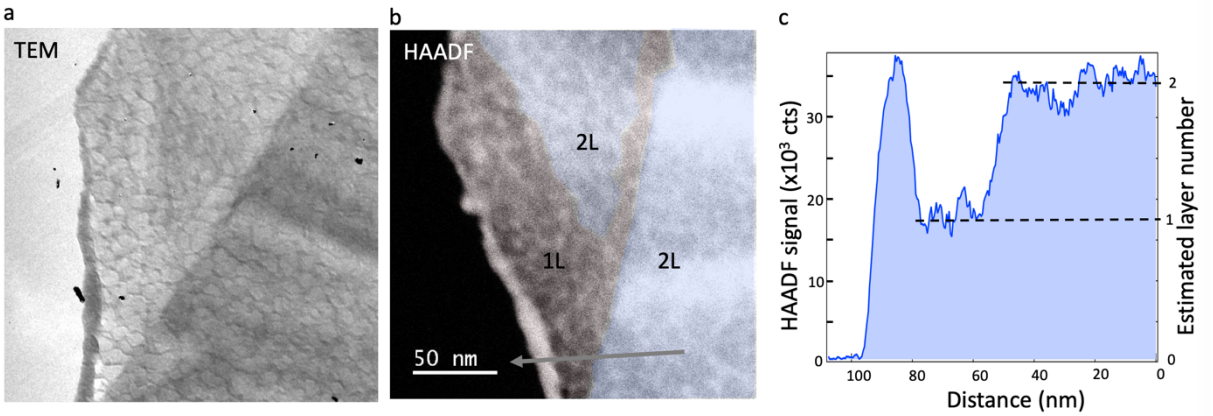

Figure S7. **a** TEM image recorded at 80 kV of an exfoliated black phosphorus flake deposited on holey carbon TEM grids. **b** HAADF image of the flake presented in **a** with a layer number indication using semi-transparent colour code based on the analysis of the HAADF profiles indicated by the numerated grey bars and presented in panel **c**. The suspended monolayer was labelled monolayer 1 for the EELS experiment.

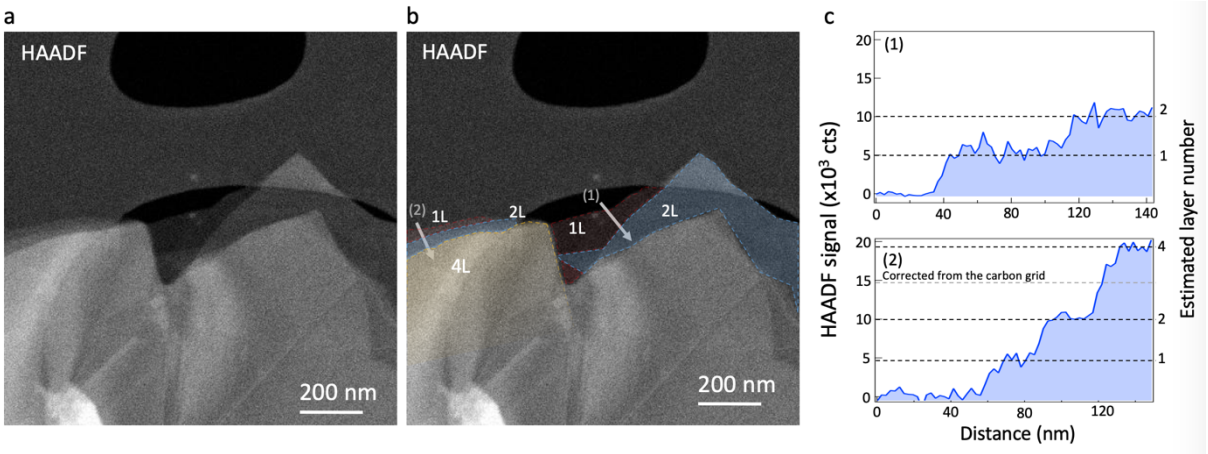

Figure S8. **a** HAADF image recorded at 80 kV of an exfoliated black phosphorus flake deposited on holey carbon TEM grids. b Same HAADF image as in **a** with a layer number indication using semi-transparent colour code based on the analysis of the HAADF profiles indicated by the numerated grey bars and presented in panel **c**. The suspended monolayer was labelled monolayer 2 for the EELS experiment.

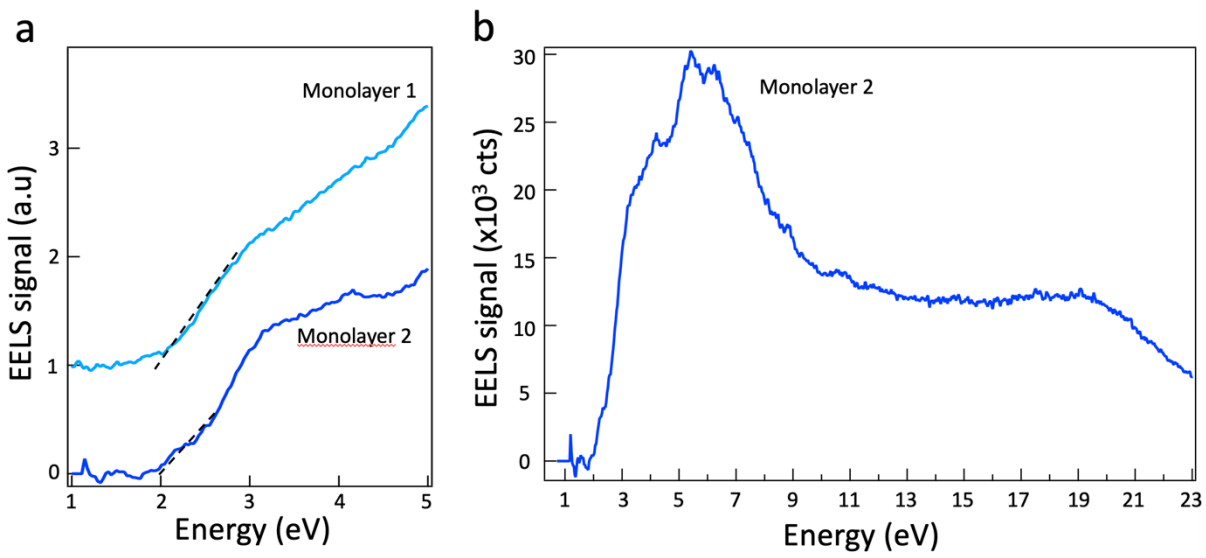

Figure S9. **a** EELS spectrum of monolayer 1 and monolayer 2 shown in Figures S1 and S2. from 0.6 eV to 4 eV. **b** EELS spectra of monolayer 2 recorded at 80kV from 0.6 eV to 23 eV. Spectra recorded at 80kV.

Table S1. Threshold values extracted from EELS spectra of mono, bi, trilayer BP presented in Figures S3, S6, S9.

BP Sample	**Near band edge threshold (eV)**	**Error (eV)**
Monolayer #1	1.9	0.1
Monolayer #2	2.0	0.1
Bilayer #1	1.4	0.1
Bilayer #2	1.5	0.1
Trilayer #1	1.1	0.15
Trilayer #2	1.1	0.15

3- Computational details (gap and binding energy)

The three free-standing structures have been relaxed with the ABINIT plane-wave code, using Troullier-Martins pseudopotentials. The Brillouin zone has been sampled with a 9x1x7 Γ-centred k-point grid, with a cut-off energy 40 Ha and the PBE approximation to the exchange-correlation potential. The tolerance in the stress tensor during structural optimization has been set to 0.0001 Ha/Bohr (~0.0007 eV/Å) per component per atom. The resulting structural parameters are summarized in Table S1.

Table S1:

	Monolayer	Bilayer	Trilayer
zigzag a (Å)	3.281	3.284	3.286
armchair c (Å)	4.609	4.579	4.571
thickness h (Å)	2.090	7.726	13.377

Once the equilibrium structure has been obtained, the Kohn-Sham Hamiltonian has been diagonalized with the GPAW code, using a cutoff energy of 700 eV (a new convergence in the cutoff was needed because GPAW uses a PAW basis). In all cases, the Coulomb truncation method has been employed and 10 Å of vacuum have been included in each simulation cell.

The Bethe-Salpeter equation (BSE) has been solved using the GPAW code, using a cutoff energy of 50 eV and a broadening constant of 0.05 eV. The other parameters of the BSE calculation and the value of the scissor operator are summarized in Table 2.

Table 2:

	Monolayer	Bilayer	Trilayer
N. bands in ε	40	80	120
N. valence bands	3	6	9
N. conduction bands	4	8	12
k-point grid (Γ-centred)	31x1x25	31x1x25	25x1x17
cell height L=V+h (Å)	12.11	17.73	23.38
Scissor operator (eV)	1.56	1.31	1.03

The scissor operator has been fixed in such a way that the optical gap extracted from the simulated loss function matches the EELS measurements of this work. This leads to

fundamental gaps of 2.46 eV, 1.90 eV and 1.34 eV in the 1-, 2- and 3-layer systems respectively. The value of the monolayer compares well with the most advanced calculations found in literature (2.4 eV obtained with Monte Carlo Methods[1] and 2.41 eV obtained with GW0+hybrid[2,3]).

The choice of vacuum in BSE calculations

It is known that simulations of isolated systems in the reciprocal space are affected by errors due to the implicit assumption of periodic boundary conditions. The introduction of an appropriately truncated Coulomb potential cures this issue permitting in addition to reduce a lot the unavoidable empty space. However, since the RPA polarizability is renormalized with respect to the volume of the cell, some arbitrariness remains in choosing how much vacuum has to be included, despite the use of the Coulomb truncation. As we show below this has severe consequences on the BSE calculation.

In Figure S1 we report test BSE spectra (not all parameters are at convergence) of the BP monolayer done with the Coulomb truncation in six cells differing by the amount of vacuum *V*. As it can be seen, despite the use of the Coulomb truncation, the first peak Ex is continuously blue-shifted as *V* is decreased, without exhibiting any convergence trend. This is highlighted in the inset by the green line, which reports Ex(1/L) in arbitrary units (L=V+h is the height of the simulation cell).

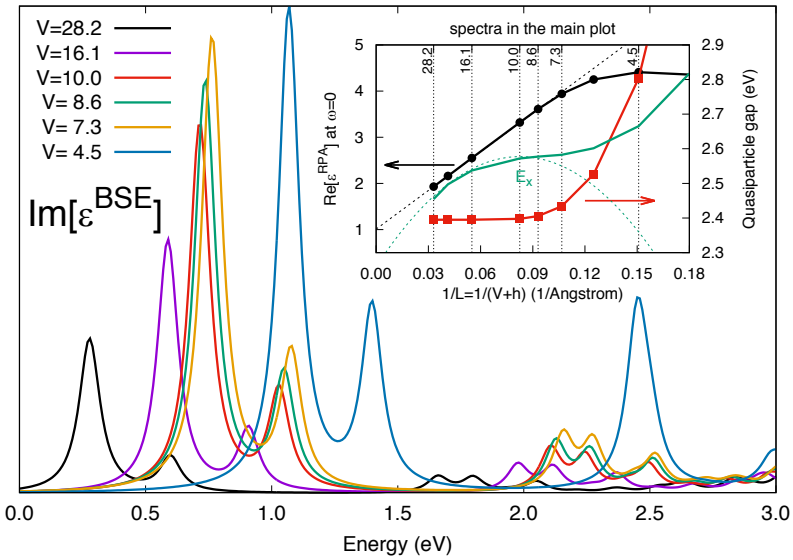

Figure S2: Body: Shift of the excitonic peak E_x in a generic 2D material (in this case a test calculation of BP monolayer) as function of the vacuum *V* included in the simulation cell. Inset: the fundamental gap $E_g(1/L)$ in red, the dielectric function $\varepsilon(1/L)$ in black and the trajectory of the excitonic peak $E_x(1/L)$ expressed in arbitrary units in green. L=V+h is the total height of the simulation cell. Lengths are in Angstrom, energies in eV.

To understand this behaviour and to specify a criterion to fix V, we have considered the variation of the dielectric function ε and of the gap E_g as function of 1/L, reported in the inset of Figure S2. Let us first focus on the black curve, the dielectric function $\varepsilon(1/L)$. For large enough cells, the dielectric function is expected to follow the linear law $\varepsilon(1/L) = 1 + 4\pi\alpha/L$ with α being the slab polarizability.[4,5] With no surprises, this is confirmed in our calculations. This means that for high-enough V, the screening entering the BSE calculation is very weak. However, in small cells (in our case starting from L=7.3 Å) the dielectric function starts deviating from the linear law bending to lower values. This is due to an artificial confinement of the electronic wave functions, as attested by the sudden increase of $E_g(1/L)$ (the fundamental gap, red curve) which instead is stable in large cells.

Combining these two elements, the continuous blue-shift of Ex can be easily explained. If too much empty space is included in the cell, the gap is at convergence, but the dielectric screening is too weak, leading to high binding energies and hence to low-energy excitons. Instead, when not enough vacuum is included, the artificially high confinement opens the gap too much and even if the exciton binding energy increases ($\varepsilon(1/L)$ bends downward), the effect does not compensate the band gap opening.

One can define the optimum vacuum V' as the amount such that $E_g(1/L)$ is converged and the linear law of the dielectric function $\varepsilon(1/L)$ still holds. In our case V'=10 Å. Because of the arguments invoked, we don't expect this value to change in the bilayer and the trilayer cases.

Anisotropic variational model of the exciton binding energy

Prada and co-workers derived a variational model for excitons in an anisotropic free-standing slab.[6]The model, based on a Wannier-Mott picture and strongly inspired by the pioneering work of Keldysh[7], provides estimations of the exciton binding energy and of the average electron-hole distance in the two directions of anisotropy. We generalised the model to take into account the effects of two sandwiching dielectrics characterised by dielectric functions ε_1 and ε_2 as in the original problem addressed by Keldysh.[7] The environment enters then in the equations through an average dielectric function $\varepsilon=(\varepsilon_1+ \varepsilon_2)/2$.

The electron-hole pair is characterised by two parameters: the effective mass μ that we obtained from our DFT calculations, and a typical screening distance $r_0 = r_0^{FS}/\varepsilon$ where r_0^{FS} is the corresponding parameter in the free-standing case. In the 1-, 2- and 3-layer we set r_0^{FS} in such a way to reproduce the binding energy predicted by our BSE simulations.

In Table 3, we report the parameter r_0 used, together with the predicted excitonic radii (a_x and a_z), and the binding energies E_b for several environmental conditions found in literature. The corresponding optical gap E_x reported in Table 3 are obtained by subtracting the simulated E_b to the measured E_g (see also main text).

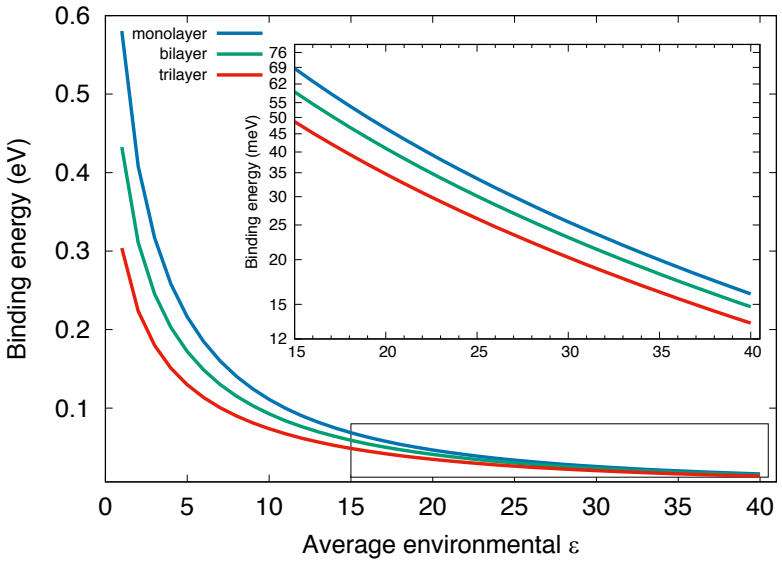

Figure S3: Variation of the binding energy E_b as function of the average dielectric function of the surroundings. Results have been obtained with the variational model.

Table S3: Results of the variational model in different environments, and comparison with experiments.[8-12] Distances are in Bohr, energies in eV. References in the Table are [14, 15, 16, 20, 21].

	$\bar{r}_0$	a_x	a_z	E_b	E_X (exp.)	E_g
$\bar{\epsilon} = 46.7$ **Liquid solvent (DMF)** (8):						
monolayer	1.99	25.09	71.49	-0.01	1.35	1.36
bilayer	2.89	27.68	75.29	-0.01	1.24	1.25
trilayer	4.50	30.61	79.07	-0.01	1.04	1.05
$\bar{\epsilon} = 36.7$ **Liquid solvent (DMSO)** (8):						
monolayer	2.53	21.07	59.58	-0.02	1.38	1.40
bilayer	3.68	23.38	62.73	-0.02	1.23	1.25
trilayer	5.72	26.32	67.20	-0.02	1.06	1.08
$\bar{\epsilon} = 32.17$ **Liquid solvent (NMP)** (9):						
monolayer	2.89	19.28	54.24	-0.02	—	—
bilayer	4.20	21.51	57.55	-0.02	1.88	1.90
trilayer	6.53	24.41	62.22	-0.02	1.43	1.45
$\bar{\epsilon} = 8.28$ **Saphire + hBN** (10):						
monolayer	11.23	10.32	27.10	-0.14	1.73	1.87
bilayer	16.30	12.28	30.72	-0.11	1.15	1.26
trilayer	25.36	15.03	35.93	-0.09	0.85	0.94
$\bar{\epsilon} = 7.0$ **Liquid solvent (CHP)** (11):						
monolayer	13.29	9.88	25.76	-0.16	1.97	2.13
bilayer	19.29	11.83	29.38	-0.13	1.33	1.46
trilayer	30.00	14.57	34.62	-0.10	1.14	1.24
$\bar{\epsilon} = 2.3$ **SiO_2** (12):						
monolayer	40.43	8.31	20.84	-0.38	1.75	2.13
bilayer	58.70	10.18	24.47	-0.29	1.29	1.58
trilayer	91.30	12.86	29.87	-0.21	0.97	1.18
$\bar{\epsilon} = 1.0$ **Free standing**:						
monolayer	93.00	7.86	19.42	-0.58	1.88	2.46
bilayer	135.00	9.70	23.04	-0.43	1.47	1.90
trilayer	210.00	12.34	28.24	-0.30	1.04	1.34

Note concerning the electronic gap calculation.

It should be stressed once more that, since it has been fixed *a posteriori* to reproduce the EELS threshold, the value of 2.4 is essentially an experimental measure. Indeed, we have used ab-initio methods more as a powerful analysis tool, than in virtue of their predictive power. Therefore, in comparing our results to other purely theoretical values reported in literature, one should avoid speculating on the reasons of possible differences, while take instead our result as an "experimental benchmark" against which theoretical methods should be tested. In this sense, our findings are consistent with the theoretical simulations of the electronic gap in the free-standing monolayer. Theoretical values range from 1.6 eV to 2.4 eV, depending on the approximations, but the two most advanced methods (Monte Carlo and

hybrid+GW_0) give both a fundamental gap of 2.4 eV (see Frank *et al.*[1] and references therein), in very good agreement with our findings.

References

(1) Frank, T.; Derian, R.; Tokár, K.; Mitas, L.; Fabian, J.; Štich. I. Many-Body Quantum Monte Carlo Study of 2D Materials: Cohesion and Band Gap in Single-Layer Phosphorene. *Phys. Rev. X* **2019,** 9, 011018

(2) Wang, V.; Kawazoe, Y.; Geng, W. T. Native point defects in few-layer phosphorene. *Phys. Rev. B* **2015,** *91,* 045433

(3) Qiu, D.; da Jornada, F. H.; Louie, S. G. Environmental Screening Effects in 2D Materials: Renormalization of the Bandgap, Electronic Structure, and Optical Spectra of Few-Layer Black Phosphorus. *Nano Lett*. **2017,** 17, 4706

(4) Cudazzo, P.; Tokatly, I. V.; Rubio, A. Dielectric screening in two-dimensional insulators: Implications for excitonic and impurity states in graphane. *Phys. Rev. B* **2011**, 84, 085406

(5) Sponza, L.; Goniakowski, J.; Noguera, C. Confinement effects in ultrathin ZnO polymorph films: Electronic and optical properties. *Phys. Rev. B* **2016**, 93, 195435

(6) Prada, E.; Alvarez, J. V.; Narasimha-Acharya, K. L.; Bailen F. J.; Palacios, J. J. Effective-mass theory for the anisotropic exciton in two-dimensional crystals: Application to phosphorene. *Phys. Rev. B* **2015**, 91, 245421

(7) Keldysh, L. V. Coulomb interaction in thin semiconductor and semimetal films *JETP Lett*. **1978**, 29, 658

(8) Yasaei, P.; Kumar, B.; Foroozan, T.; Wang, C.; Asadi, M.; Tuschel, D.; Indacochea, J. E.; Klie, R. F.; Salehi-Khojin, A. High-Quality Black Phosphorus Atomic Layers by Liquid-Phase Exfoliation. *Adv. Mater.* **2015**, 27, 1887

(9) Woomer, A. H.; Farnsworth, T. W.; Hu, J.; Wells, R. A.; Donley, C. L.; Warren, S. C. Phosphorene: Synthesis, Scale-Up, and Quantitative Optical Spectroscopy. *ACS Nano* **2015**, 9, 8869

(10) Li, L.; Kim, J.; Jin, C.; Ye, G. J.; Qiu, D. Y.; da Jornada, F. H.; Shi, Z.; Chen, L.; Zhang, Z.; Yang, F.; Watanabe, K.; Taniguchi, T.; Ren, W.; Louie, S. G; Chen, X. H.; Zhang, Y.; Wang, F. Direct observation of the layer-dependent electronic structure in phosphorene. *Nat. Nanotech*. **2016**, 12, 21

(11) Hanlon, D.; Backes, C; Doherty, E.; Cucinotta, C. S.; Berner, N. C; Boland, C.; Lee, K.; Harvey, A; Lynch, P; Gholamwand, Z.; Zhang, S.; Wang, K; Moynihan, G; Pokle, A; Ramasse, Q. M.; McEvoy, N.; Blau, W. J.; Wang, J.; Abellan, G.; Hauke, F; Hirsh, A; Sanvito, S.; O'Regan, D. D; Duesberg, G. S; Nicolosi, V; Coleman, J. N. Liquid exfoliation of solvent-stabilized few-layer black phosphorus for applications beyond electronics. *Nature Comm*. **2015**, 6, 8563

[12] Yang, J.; Xu, R.; Pei, J.; Myint, Y. W; Wang, F; Wang, Z.; Yu, Z.; Lu, Y. Unambiguous identification of monolayer phosphorene by phase-shifting interferometry. *ArXiv* **2014**, 1412:6701